The Mantis Shrimp Saddle: A Biological Spring Combining Stiffness and Flexibility

*Maryam Tadayon, Shahrouz Amini, Admir Masic, and Ali Miserez**

Stomatopods are aggressive crustacean predators that use a pair of ultrafast raptorial appendages to strike on prey. This swift movement is driven by a power amplification system comprising components that must be able to repetitively store and release a high amount of elastic energy. An essential component of this system is the saddle structure, in which the elastic energy is stored by bending prior to striking. Here, a comprehensive study that sheds light on the microstructural and chemical designs of the stomatopod's saddle is conducted. MicroCT scans combined with electron microscopy imaging, elemental mapping, high-resolution confocal Raman microscopy, and nanomechanical mapping show that the saddle is a bilayer structure with sharp changes in chemical composition and mechanical properties between the layers. The outer layer is heavily mineralized whereas the inner layer contains a high content of chitin and proteins, leading to a spatial organization of phases which is optimized for load distribution during saddle bending. The mineralized outer layer sustains compressive stresses, whereas the inner biopolymeric layer provides tensile resistance. These findings reveal that the saddle chemical composition and microstructure have been spatially tuned to generate a stiff, yet flexible structure that is optimized for storage of elastic energy.

1. Introduction

Stomatopods (commonly called "mantis shrimps") are an ancient group of ambush predatory marine crustaceans.[1] Their raptorial appendages have emerged in recent years as an exciting model structure in bioinspired material engineering.[2–4] Depending on the species, stomatopods are equipped with either a "smasher"[5] or with a "spearer" dactyl club appendage.[6] The former is used as a tough hammer to shatter hard shells, whereas the latter is deployed to quickly grasp unexpecting softer body prey. To perform these mechanically intensive tasks, stomatopods have evolved complex multiscale structural and crystallo-chemical designs that endow their clubs with a remarkable damage tolerance. Notably, the clubs are made of distinct regions consisting of an outer impact layer, an inner softer region, and a nested region.[3] The impact layer contains both crystalline and amorphous calcium phosphate. Textured crystalline Fluorapatite (FAP) is the dominant phase near the impact surface, whereas amorphous calcium phosphate (ACP) is more abundant near the interface with the inner region. The inner region is less mineralized and is comprised of partially mineralized chitin fibers decorated with amorphous calcium carbonate (ACC), which assemble into a helicoidal composite structure. Microchannels running perpendicular to the main club axis and required for diffusion of inorganic ions and mineral deposition during club growth are also present in the inner layers. Recent contact mechanics studies have demonstrated that this microstructural design, which has been detected in both species, leads to distinct micromechanical responses in the layers,[4] namely, quasi-plasticity and high compressive yield strength in the outer layers and strain-hardening in the inner layers, which synergistically combine to endow the club with a remarkable impact tolerance.

Common to both species is the fast velocity at which the appendages are deployed during a strike, although the smasher strikes quicker than the spearer, in the range of 14–23 m s^{-1} (see Patek et al.[5]) versus ≈4.5–7 m s^{-1} for the spearer.[6] Early work suggested that the potential elastic energy could be stored in the extensor muscle and apodeme.[7] Patek and co-workers[8–12] later pointed out that the energy required to trigger these ultrafast raptorial movements cannot be supplied by muscles alone. Hence, this group suggested the presence of a strong and effective spring, called the "saddle", which is located on the dorsal top of the merus segment and acts as a discrete structure that stores the elastic energy for strike.[5] Further complementary studies revealed that the strike is driven by a complex power amplification mechanism located in the merus and comprising hard, soft, and connective tissues that all work in concert to amplify the power and speed of the strike.[13,14]

M. Tadayon, S. Amini, Prof. A. Miserez
Biological and Biomimetic Materials Laboratory
School of Materials Science and Engineering
50 Nangang Avenue
Nanyang Technological University
639798, Singapore
E-mail: ali.miserez@ntu.edu.sg
Dr. A. Masic
Max Planck Institute of Colloids and Interfaces
Potsdam 14424, Germany
Prof. A. Miserez
School of Biological Sciences
60 Nanyang Drive
Nanyang Technological University
637551, Singapore

DOI: 10.1002/adfm.201502987

These studies have revealed the various sources of storing-energy mechanisms during a striking cycle, including flexing of the merus exoskeleton to restore the energy, rotation of the meral-V, flexing of the ventral bars acting as tape springs, and the compression and expansion of the saddle.[10,13,14] While a detailed picture of the kinematic mechanisms involved during energy storage and release is currently still being refined, there are evidences that among these coupled structures the saddle is likely the stiffest and plays a central role in storage of elastic energy, with a mechanism that remains highly similar between the smasher and the spearer species.[5,7,12] As a hyperbolic-paraboloid structure located in the dorsal part of the merus, the saddle is fixed along its longitudinal direction to the hard shell of the merus, and is flanked with a soft and flexible membrane on its sides (**Figure 1**). Although the color and size vary from species to species, the geometrical characteristics of the saddle remain essential identical in all species.[12,13]

In order to maximize the impact energy, the saddle must store a high amount of elastic energy, i.e., its spring constant must be high and it must exhibit substantial elastic flexibility. Ideally, this requires stiff building blocks that are capable of being elastically deformed, yet not too brittle in order to prevent internal damage during deformation, which would seriously undermines repetitive usage. This provides an "engineering" challenge because high stiffness and flexibility are generally viewed as mutually exclusive properties of structural materials, including biological materials.[15–17] According to large-scale microCT observations,[14] the saddle has been suggested to be partially mineralized, which would fit the first requirement since mineralized phases are stiffer than biopolymers. At the same time, minerals are more brittle—especially in tension—and much less extensible than most unmineralized structures, which would thus fail the second requirement.[18] However, a detailed materials analysis and microstructural study of the saddle structure has so far not been undertaken, such that the actual degree of mineralization and identity of the mineral phases of the saddle remain open questions.

In this work we sought to elucidate this apparent dichotomy by characterizing the chemical composition and spatial distribution of the constitutive phases of the saddle, as well as its larger scale microstructural design. In parallel, we conducted micrometer-scale nanomechanical mapping of the saddle in order to establish structure properties relationships. Such studies have previously not been conducted and we reasoned that obtaining details about the mineral content and their spatial distribution would provide a better understanding of the saddle functionality. Our results demonstrate that the saddle spring is a multiphase biocomposite with an organic/inorganic composition ratio that is spatially tuned along the saddle cross-section. During elastic energy storage, the individual phases are mechanically loaded to take advantage of their intrinsic mechanical properties. Thus, the outer layer—subjected to compressive loading during bending—is more mineralized, whereas the inner layer, which sustains tensile stresses during bending, is predominantly biopolymeric.

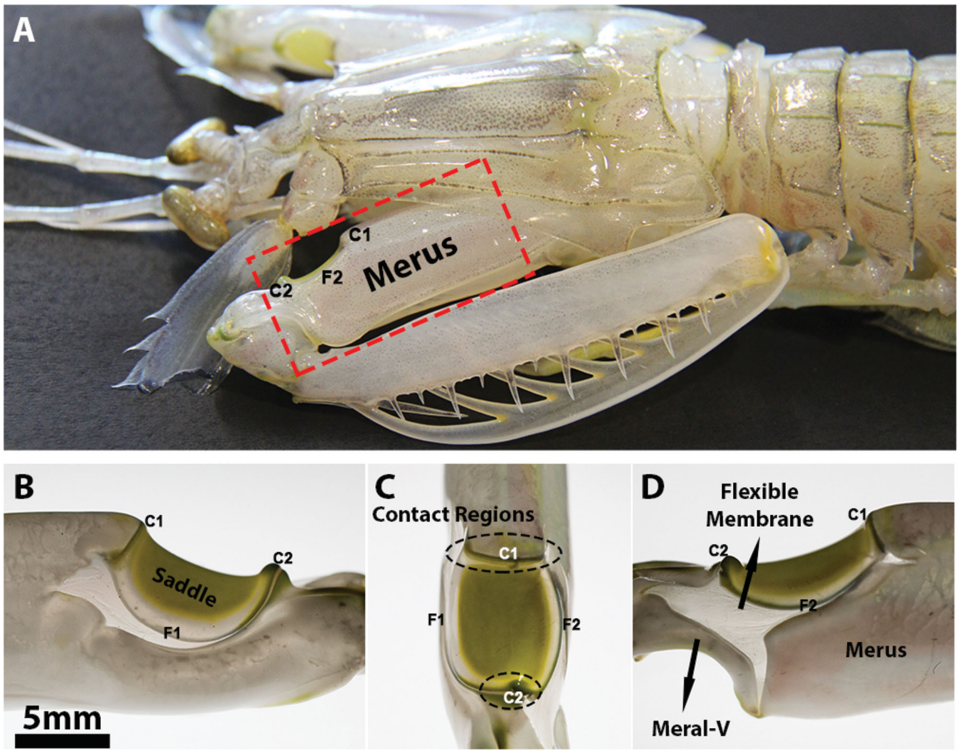

Figure 1. Photographs of Harpiosquilla Harpax stomatopod's feeding appendage. A) Merus in the upper part of the appendage. B) Medial view of the saddle in the merus. C) Top view of the merus, the saddle, and the rigid contact regions. D) The saddle and meral-V positions in the merus from the lateral view. (C1, C2) and (F1, F2) indicate the contact points and free edges, respectively.

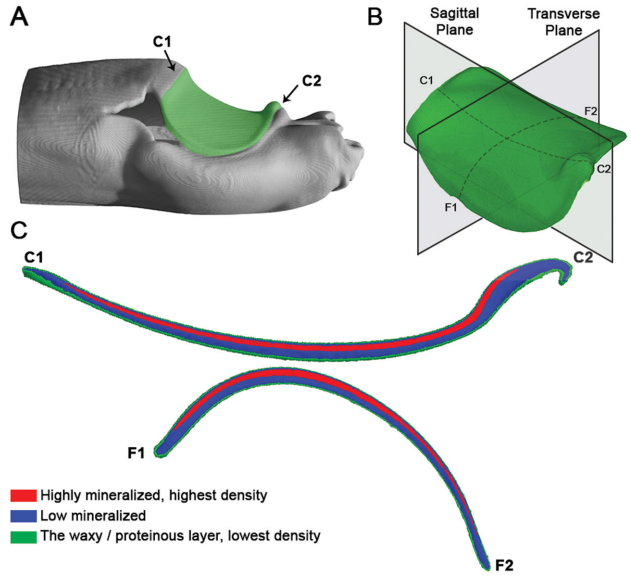

Figure 2. MicroCT scan of a saddle. A) MicroCT image of the whole saddle (in green) illustrating its position in the merus. C1 and C2 points are fixed points through which the compressive force is transmitted in the native saddle. B) Mutually perpendicular cross-sections planes subsequently used to visualize mineral distribution. C1–C2 is the sagittal plane and F1–F2 the transversal plane. C) MicroCT cross-sections as defined in (B) with filtered density distribution. The outer layer is denser (highly mineralized, red), whereas the inner layer is less dense (weakly mineralized, blue). Toward the edges of the saddle, the outer (highly mineralized) layer vanishes. The thin green region corresponds to the wax, waterproof coating.

2. Results

2.1. Macroscopic Features and Saddle Microstructure

Macro-photo images displayed in Figure 1 illustrate the characteristic hyperbolic-paraboloid shape of the saddle, which is elongated along the longitudinal axis of the body. The saddles' sizes varied from 6.7 ± 1.5 mm in length and 5.9 ± 1.3 mm in width (n = 25). In order to visualize the overall mineral distribution in the structure, a whole saddle structure was probed by microCT. The resulting 3D scan is shown in **Figure 2**A, where the location of the fixed points C1 and C2 is also highlighted. Cross-section images were then generated from the 3D scan across mutually perpendicular planes, namely the sagittal (C1–C2) and the transversal (F1–F2) planes, as illustrated in Figure 2B. In these sections, the phase contrast was obtained by filtering the CT scan with the mass density, such that light regions are color-coded in blue while denser regions appear in red (Supporting Information, Figure S1). This density contrast clearly indicates that the saddle is comprised of two distinct layers: an outer, denser layer, and an inner layer with a lower mass density. While the overall thickness of the saddle remains constant (346 ± 58 µm; n = 25), the relative thickness of both layers is not uniform across the saddle. The inner layer expands toward the external edges, whereas the thickness of the outer layer gradually decreases away from the center of the saddle and eventually vanishes at the free edges. This feature is observed for both cross-sectional planes. Furthermore, a very thin layer 5 to 8 µm thick (which is about 1% to 2% of the whole thickness of the saddle) is observed on the free surface of the saddle (Figure 2C). As described later, this thin layer is non-mineralized and is suggested to serve as a waterproof protective layer, very similar to the role of waxy epicuticle in arthropod cuticles[19] (Supporting Information, Figure S2A).

Smaller scale microstructural features were obtained by field emission scanning electron microscopy (FESEM). Low-magnification images of sagittal and transverse cross-sections, consisting of 20 FESEM images assembled together, are depicted in **Figure 3**A,B, where the outer (denser) layer is highlighted in red for clarity. A higher magnification image near the central region and encompassing the full thickness reveals that both layers are microstructurally distinct. The outer layer is more compact and exhibits a smoother overall appearance. As detected on the CT scans, it is thicker in the middle, becomes thinner toward the edges (Figure 3D), and finally disappears near the contacts points. The inner layer, on the other hand, exhibits a periodic sheet-like structure, with the thickness of the sheets (as represented by their periodic wavelength, λ) gradually decreasing toward the innermost region of the saddle. Fractured cross-sectional images of the saddle are depicted in Figure 3E (low magnification image) and Figure 3F–G (higher magnification images) and provide additional information about the layers' microstructures. The outer layer (Figure 3F) contains compact microtubules generally oriented perpendicular to the free surface. In contrast, microfibrils are stacked into sheets in the inner layer. The microfibril orientation in these sheets is parallel to the free surface and this preferred orientation gradually varies between sheets. These sub-layers thus exhibit the classical "Bouligand-like" twisted plywood structure previously observed in the stomatopod's dactyl clubs[3] and in other crustacean exoskeletons.[20–22]

2.2. Chemical Composition and Spatial Distribution

2.2.1. Inorganic and Organic Spatial Distribution

A low magnification FESEM image of a saddle cross-section is depicted in **Figure 4**A. Raman spectra profiles and chemical images were subsequently acquired at various points along this cross-section, which were located either in the outer or in the inner layers. Raman spectra (Figure 4B) reveal significant differences between the layers, especially with regard to the relative intensities of the main bands. In the outer layers, four bands are observed at wavenumbers of 963 cm^{-1}, 1085 cm^{-1}, 1600–1700 cm^{-1}, and 2860–2940 cm^{-1}, which can be attributed to phosphate, carbonate, amide I (proteins), and C–H stretching of organic matrix (mainly chitin), respectively,[23] with the phosphate and carbonate bands being clearly the most intense. Two other sharp peaks at 1156 and 1520 cm^{-1} are attributed to carotenoid, an organic pigment responsible for the green or orange color of the saddle.[23] The broad bands (band width in the range of 30 cm^{-1}, see Supporting Information, Figure S3) associated with the phosphate and carbonate vibrations imply that these phases are amorphous, thus corresponding to ACP and ACC, respectively.[24] Furthermore, the position of the ACC

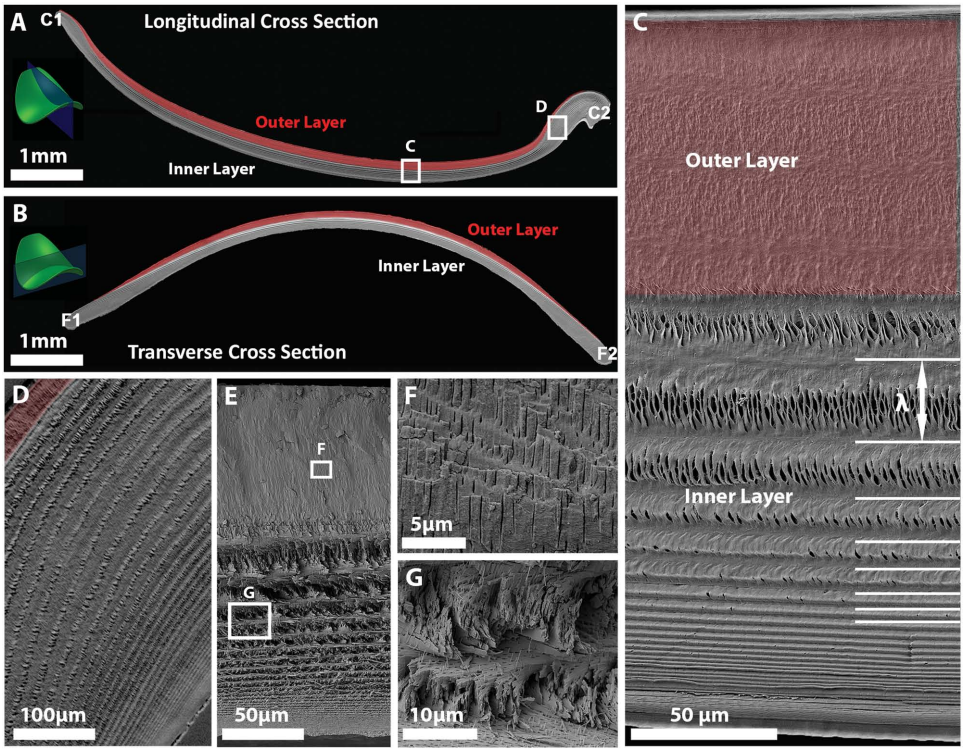

Figure 3. FESEM images of a mantis shrimp saddle. A) Low-magnification sagittal, and B) transversal cross-sections of a whole saddle (C1, C2, F1, and F2 are defined as in Figures 1 and 2) each obtained by stitching 20 individual FESEM images. The red highlighted region indicates the outer highly mineralized layer. C) Polished and urea-etched transverse cross-section near the center of the saddle, showing microstructural distinctions between each layer. λ is the periodic distance of the plywood structure in the inner layers. D) Decrease of the outer layer thickness close to the contact regions. E) Fractured surface of the saddle. F) Higher magnification image of the outer layer illustrating the presence of microtubuluar elements in the compact outer surface. G) Higher magnification of the inner layer, showing the presence of sub-micrometer fibrous elements arranged in a helicoidal "Bouligand" pattern.

Raman peak suggests around 30% magnesium (Mg) substitution in the carbonate phase[25,26] whereas the ACP peak position indicates that the phosphate phase is fluorinated in the form of amorphous FAP.[2] In the inner layers, the intensities of mineral phase bands are much smaller and similar to those arising from the organic matrix. Here, the peaks in the ranges 1600 to 1700 and 2800 to 3000 cm^{-1} correspond to proteins and organic matrix in general, respectively,[23] whose relative abundance are clearly higher in the inner layers of the saddle.

Visualization of the spatial distribution of these phases was achieved by imaging the major inorganic (ACP and ACC) and organic bands (Amide I and chitin) by polarized confocal Raman microscopy, as shown in Figure 4C. The images distinctly indicate that mineral phases are mainly localized in the outer layer, while the inner layers are predominantly organic. This pattern was corroborated by treating the saddle with 0.1 M ethylenediamineteteraacetic acid (EDTA) for 12 h and by comparing FESEM images of the sample before and after treatment (Figure 4D). EDTA treatment led to complete removal of the outer layer. The inner layer, on the other hand, remained mostly intact, although some shrinkage was noticed. By rotating the polarization of the incident laser light from 0° to 90° the anisotropy of the chitin-protein network is clearly observed (Figure 4C, green).[27] The banding pattern oberved in the confocal Raman images is also consistent with the fibril organization into a classical helicoidal (Bouligand) structure, whereby the preferred fibril orientation rotates from layer to layer, as evidenced in the SEM image shown in Figure 3G. Indeed, under the polarized laser beam the scattering intensity of the associated Raman shifts varies as a function of the fibril/polarization angle. Fibrils oriented perpendicular to the cross-section give rise to a higher intensity of their Raman band in comparison to fibers oriented parallel to the cross-section. The Raman spectrum of the outermost thin layer (Supporting Information, Figure S2) indicates that this layer contains more carotenoid in comparison with the outer and the inner layers. Furthermore, the presence of C–H stretching in the range 2850–3000 and ≈2600–2700 cm^{-1} is consistent with the presence of alkanes and fatty acids[28] which are typical components of waxes, though the exact composition remains unknown.

Next, we conducted elemental analysis of a saddle cross-section by energy X-ray dispersive spectroscopy (EDS). Both point spectra on different regions and elemental mapping of a whole section were obtained (**Figure 5**A,B). Elemental mapping shows high contents of calcium (Ca) and phosphorous (P) in the outer layer, in agreement with the presence of calcium carbonate and calcium phosphate detected by Raman spectroscopy. Another salient feature of the outer layer is its enrichment in Mg. Mg has been established to stabilize amorphous phases in biominerals,[29,30] which is again fully consistent with the amorphous

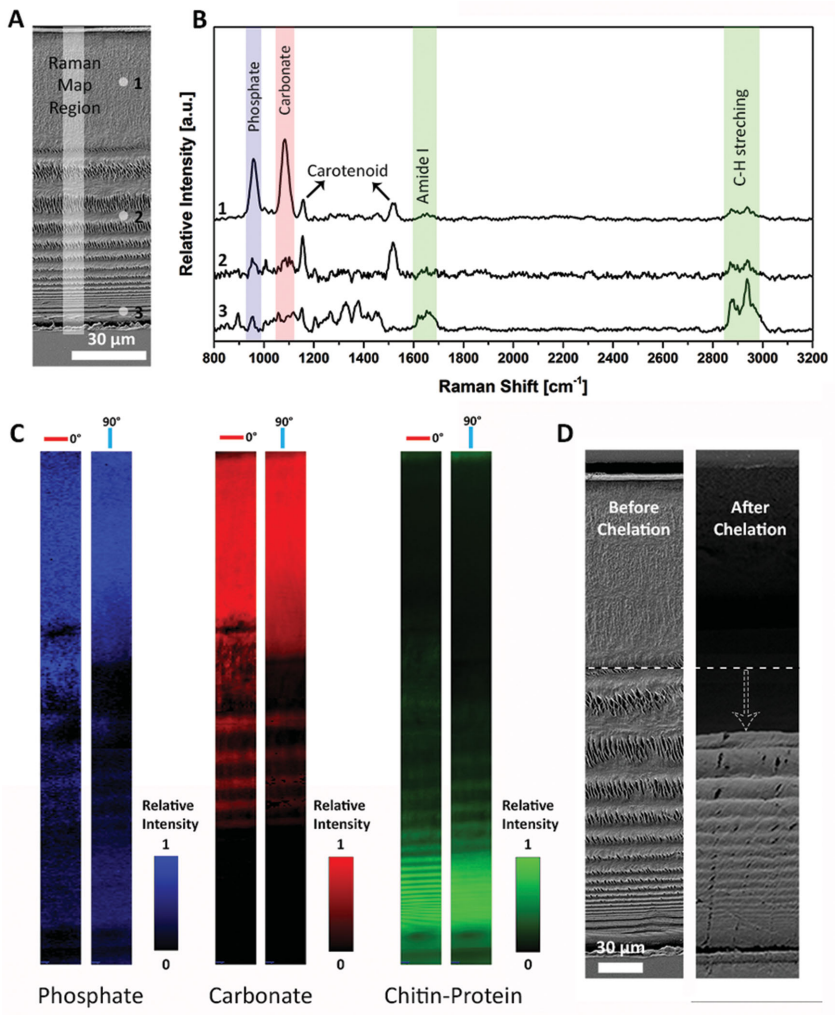

Figure 4. Raman spectra profiles and confocal imaging of a saddle cross-section. A) FESEM of a saddle displaying the point locations for Raman spectra and the region for Raman imaging. B) Raman spectra in the range of 800–3200 cm^{-1} showing the major bands attributed to phosphate, carbonate, carotenoids, Amide I (proteins), and C–H stretching (mainly chitin). C) High resolution Raman images normalized and filtered for bands centered at 963 cm^{-1} (phosphate), 1085 cm^{-1} (carbonate), and 2810–2980 cm^{-1} (chitin-protein). D) FESEM image of a saddle cross-section before (left) and after (right) incubation in 0.1 M EDTA for 12 h. EDTA incubation led to full removal of the outer layer and shrinkage of the inner layer.

state of these phases as suggested by the width of the Raman peaks and with their location corresponding to Mg-substituted ACC (Figure 4B). On the other hand, these elements are much less abundant in the inner layer, which is instead enriched in carbon (C). Point spectra (Figure 5C) further indicate that the decrease in Ca, P, and Mg is gradual from the outer to the inner layer. Taken together, Raman and EDS data unambiguously show that the saddle outer layer is mineralized with ACP and ACC, whereas the degree of mineralization decreases in the inner layer, which is predominantly organic. To assess the relative weight fraction of organic and inorganic phases in each layer as well as their water content, the individual layers were carefully separated and subjected to thermal gravimetric analysis (TGA) (Supporting Information, Figure S4). In the outer layer, the water content is 14 wt%, whereas for the inner layer the water content is 31 wt%. In the dry state (namely after removing the weight contribution from water), the mineral to organic weight ratio is 84:16 for the outer layer and 50:50 for the inner layer (Supporting Information, Table S1).

2.2.2. Organic Composition

In order to elucidate the chemical composition of the organic phases present in the saddle, Fourier Transform Infrared (FTIR) spectroscopy and quantitative Ninhydrin-based amino acid analysis (AAA)[31] measurements were conducted on a demineralized saddle (**Figure 6**A,i). The main bands of FTIR spectra correspond to Amide I and II and to polysaccharides, consistent with the presence of proteins and chitin, respectively. Zoom-in on the polysaccharide band (Figure 6B) and comparison with α- and β-chitin from the literature[32] allows us to conclude that α-chitin is the polymorphic chitin phase of the saddle.

The demineralized saddle was further treated in a solution of 5% acetic acid/8 M urea and the soluble fraction analyzed by FTIR. The spectrum (Figure 6A,ii) shows that the intensity of chitin peaks nearly vanishes, indicating that proteins and chitin can be separated by this method. AAA profiles of a demineralized saddle are displayed in Figure 6C. Comparing the whole saddle with a glucosamine (GA) standard—the hydrolysis product of chitin—indicates that GA has the same elution time as Histidine (His), which would preclude accurate amino acid quantification given the high abundance of chitin in the saddle. Therefore, quantitative AAA was conducted on a demineralized saddle that was subsequently incubated in 5% acetic acid/8 M urea (soluble fraction) since this treatment selectively separates chitin from proteins (Figure 6A,ii). Treatment with alkali peroxide (mixture of H_2O, 30% H_2O_2, and 10N NaOH, with volume percentages of 92.5%, 5%, and 2.5%, respectively) was also used as an alternate method to separate proteins from chitin[33] and identical results were obtained. A representative AAA spectrum of the protein hydrolysate following chitin removal is shown in Figure 6C (spectrum v), with the quantitative analysis presented in **Table 1**. The data indicate an amino acid composition dominated by hydrophobic residues, notably alanine (Ala), glycine (Gly), and valine (Val), which together account for 35 mol%. of the total amino acid composition. Another noticeable feature pertains to the relatively high abundance of acidic residues, with aspartic acid (Asp) and glutamic acid (Glu) combining to ≈17 mol% of the total amino acid composition. Acidic proteins are well-known to play an important role in biomineralization processes.[34,35] For instance phosphorylated proteins

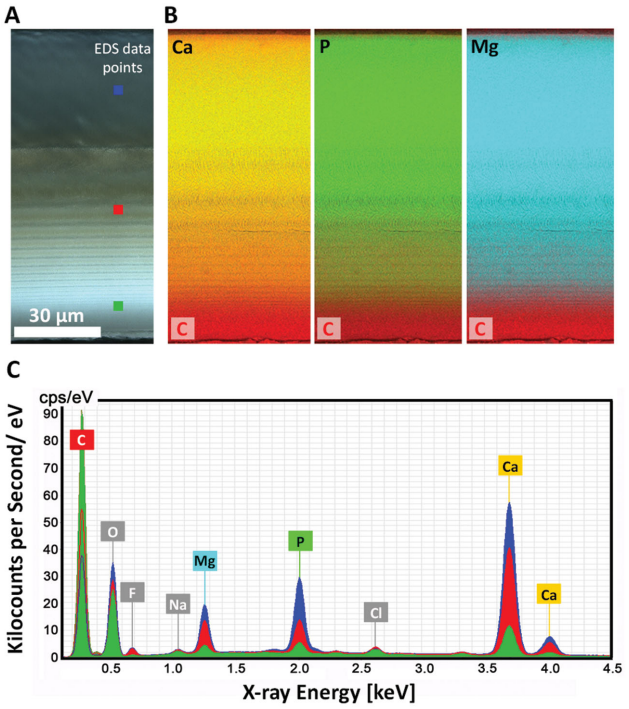

Figure 5. EDS elemental maps of a sectioned and polished saddle. A) Optical image revealing the layers and presenting the region and points for EDS maps and spectra, respectively. B) High resolution elemental maps of calcium (Ca, yellow), phosphorous (P, green), and magnesium (Mg, magenta). In each map, carbon (C) content is shown in red. C) Point spectra acquired in different positions along a saddle cross-section, showing both major major (top) and minor (bottom) elements.

such as osteopontin in bone are important to regulate apatite mineralization during bone formation.[36] Similarly the Pif shell matrix protein has been shown to regulate calcium carbonate crystallization during nacre formation,[37] and we suggest that similar proteins account for the abundance of acidic residues detected in proteins extracted from the saddle. We also conducted FESEM observations of the saddle structure following EDTA and alkaline peroxidation treatments, after which only chitin remains (Figure 6B, inset). This image demonstrates that the residual chitin phase has an overall microstructure that is very similar to that prior to selective dissolution (Figure 3), suggesting that chitin forms the scaffold of the helicoidal bouligand structure, which is subsequently decorated by the mineral phase.

2.3. Micromechanical Properties and Macroscopic Mechanical Response

Mechanical properties mapping of the saddle for both species were obtained by nanoindentation in both dry and wet conditions (comparison between species shown in Figure S5, Supporting Information). These measurements show that the two layers exhibit significant differences, with the outer layer in dry conditions having a higher elastic modulus ($E_{r,dry}$ = 33.7 ± 0.3 GPa) and hardness (H_{dry} = 1.31 ± 0.03 GPa) than the inner layer ($E_{r,dry}$ = 10.1 ± 0.1 GPa; H_{dry} = 64 ± 9 MPa)

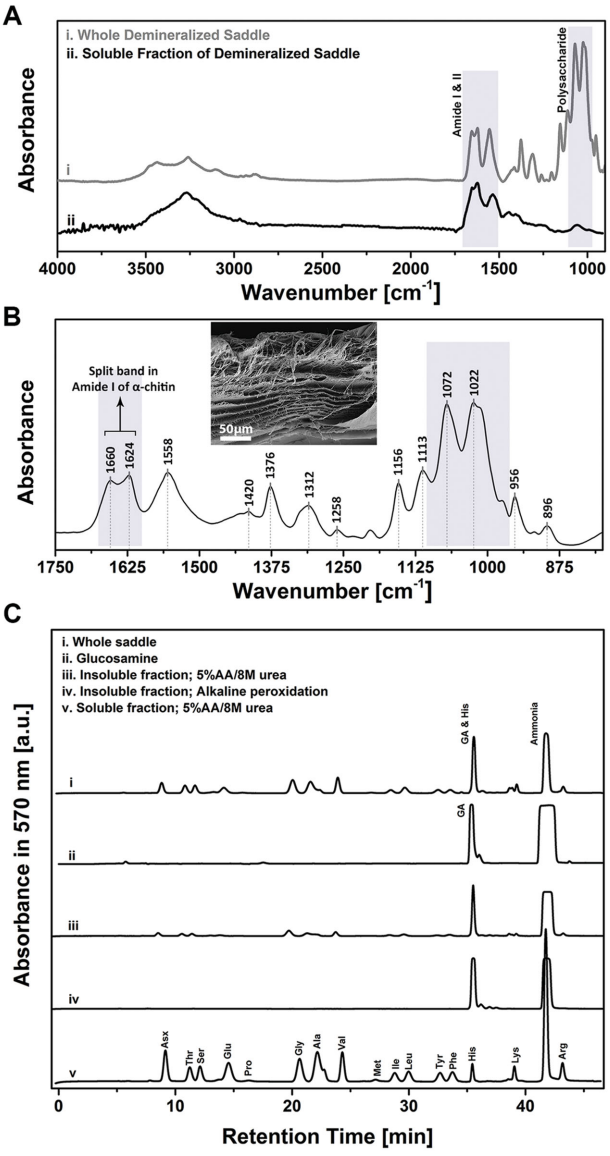

Figure 6. Biochemical analysis of saddle. A) Fourier transform infrared (FTIR) spectra of saddle before and after protein/chitin separation. B) Zoom-in in the 1750–900 cm^{-1} region of the insoluble (protein-free) fraction. Doublet peaks (1660 and 1624 cm^{-1}) in the Amide I region as well as the 1022 cm^{-1} peak are characteristics of α-chitin.[32] C) Amino acid analysis of (i) the whole saddle, (ii) a glucosamine (GA) standard corresponding to the hydrolysis product of chitosan, (iii) the insoluble fraction after 5% acetic acid/8 M urea treatment, (iv) the insoluble fraction of alkali peroxidation treatment, and (v) the soluble fraction after 5% acetic acid/8 M urea treatment. The inset in (B) is a FESEM image after both EDTA and alkaline peroxidation treatments (selective dissolution of both minerals and proteins), showing the general structure of chitin fibrils.

(**Figure 7**A). Both values sharply drop at the interface, but in contrast to the dactyl club[2,4] or many other biotools,[38] the mechanical response remains essentially homogenous within the individual layers. The mechanical contrast between the two layers is amplified under hydrated conditions (Figure 7A,B). Thus for the outer layer, the modulus drops sixfold from dry to

Table 1. Amino acid composition of the proteins in the saddle in mole percent.

Amino acid	mol%	Amino acid	mol%
Ala	14.5	Thr	4.7
Gly	10.1	Leu	4.4
Val	9.5	Phe	4.3
Asx	8.8	Tyr	3.9
Glu	8.1	Ile	3.7
Arg	6.4	Lys	3.6
Pro	5.5	His	3.5
Ser	4.9	Others	4.1

hydrated conditions ($E_{r,hydrated}$ = 5.02 ± 0.02 GPa), whereas the drop is 11-fold for the inner layer ($E_{r,hydrated}$ = 0.92 ± 0.06 GPa). These trends are fully consistent with the higher content of chitin/protein organic complex in the inner layer, since the mechanical response of biopolymers is well-established to be more susceptible to hydration than heavily mineralized phases.[18,38] It should also be mentioned that the mechanical properties of the outermost, waxy coating is orders of magnitude lower than the other layers, which is consistent with a water barrier role[39] as opposed to a structural role.

In the native merus, the compressive forces generated by the extensor muscle[13,14] are transmitted to the saddle in the longitudinal direction (Figure 1C) through the contact points C1 and C2. In order to study the saddle's macroscopic response to native compression when the animal is storing energy prior to its strike, we subjected saddles to compressive testing using a custom made universal micro-testing machine. Saddles were fixed at both contact points (C1 and C2) and the load was applied longitudinally (**Figure 8**A). The axial displacement was measured with a linear variable displacement transducer (LVDT) while the transverse displacement was simultaneously monitored along the F1–F2 direction (Figure 8A) at regular load intervals using a digital micrometer. As the saddle is longitudinally compressed, it concomitantly expands laterally, leading to an overall flattening of the structure as schematically illustrated in Figure 8B. Representative curves are shown in Figure 8C, which display the longitudinal force versus the normalized displacement in both the longitudinal and the transverse direction. The average spring constant k was found to be 143.6 ± 31.8 N mm^{-1} (Figure 8D) and we did not observe statistical differences for the spring constant as a function of size within the range of saddle size tested ($p > 0.1$, Supporting Information, Figure S6). Similarly, there was no statistical difference in spring constant between the spearer and the smasher species. For a given load, the lateral expansion was found to be about 2.5-fold greater than the longitudinal contraction. In terms of stress distribution, an imposed bending along the sagittal plane (C1–C2) leads to compressive stresses in the outer layers and to tensile stresses in the inner layers for most the of the saddle cross-sections (Figure 8E). However, the saddle geometry imposes an overall more complex loading state: since the saddle extremites along the transversal plane (F1–F2) expand (Figure 8F), the outer layers near these extremities must also be under tensile stress. Based on our compression test on hydrated samples, we suggest that the saddle can be compressed up to 2%–3% in the longitudinal direction without any damage or failure. The stored elastic potential energy E_p in the saddle can be simply calculated from the area under the load-displacement P-δ graph (Figure 8D) or using the simple equation $E_p = \frac{1}{2}k\delta^2$. Considering the maximum elastic compression taking place at 25–40 N of force and a spring constant k of 143.6 ± 31.8 N mm^{-1}, the elastic potential energy stored in the saddle is $\approx E_p = 1.29 \pm 0.28$ J.

3. Discussion

Mantis shrimps utilize a well-developed mechanical amplification system for their raptorial appendage, which is employed to magnify the relatively small mechanical power generated by their muscle in order to generate their powerful, ultrafast strikes. This amplification system contains muscles, tendons, linkages, the saddle, the meral-V, and ventral bars, which all synergistically contribute to amplify the extensor muscle power to accelerate the raptorial appendage.[11] The saddle is among the stiffest part of this complex amplification system and is designed to store, and later release, the elastic energy by flexing in the longitudinal direction (Figure 8). Virtually all biological materials are composite structures,[15,40] with hierarchical

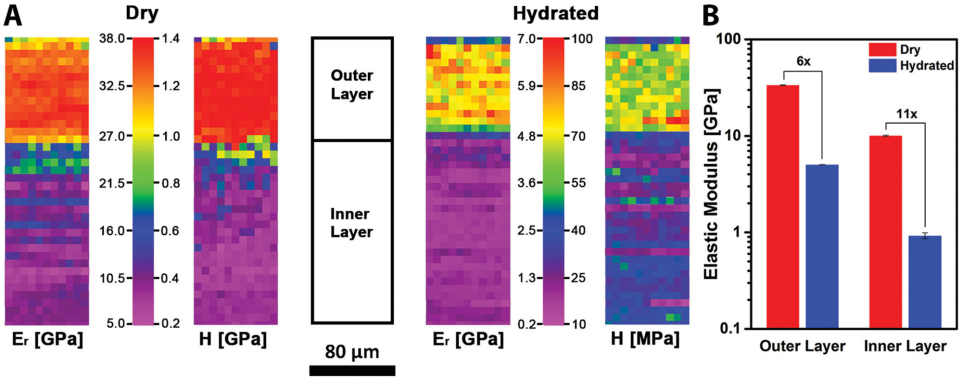

Figure 7. Mechanical properties of the saddle obtained by nanoindentation. A) High-resolution reduced elastic modulus (E_r) and Hardness (H) mapping of a saddle cross-section in dry (left) and hydrated (right) conditions. B) Average E_r values for the outer and the inner layers in both dry and hydrated conditions. The properties drop under hydrated conditions is more marked for the inner (11-fold) than for the outer (6-fold) layer.

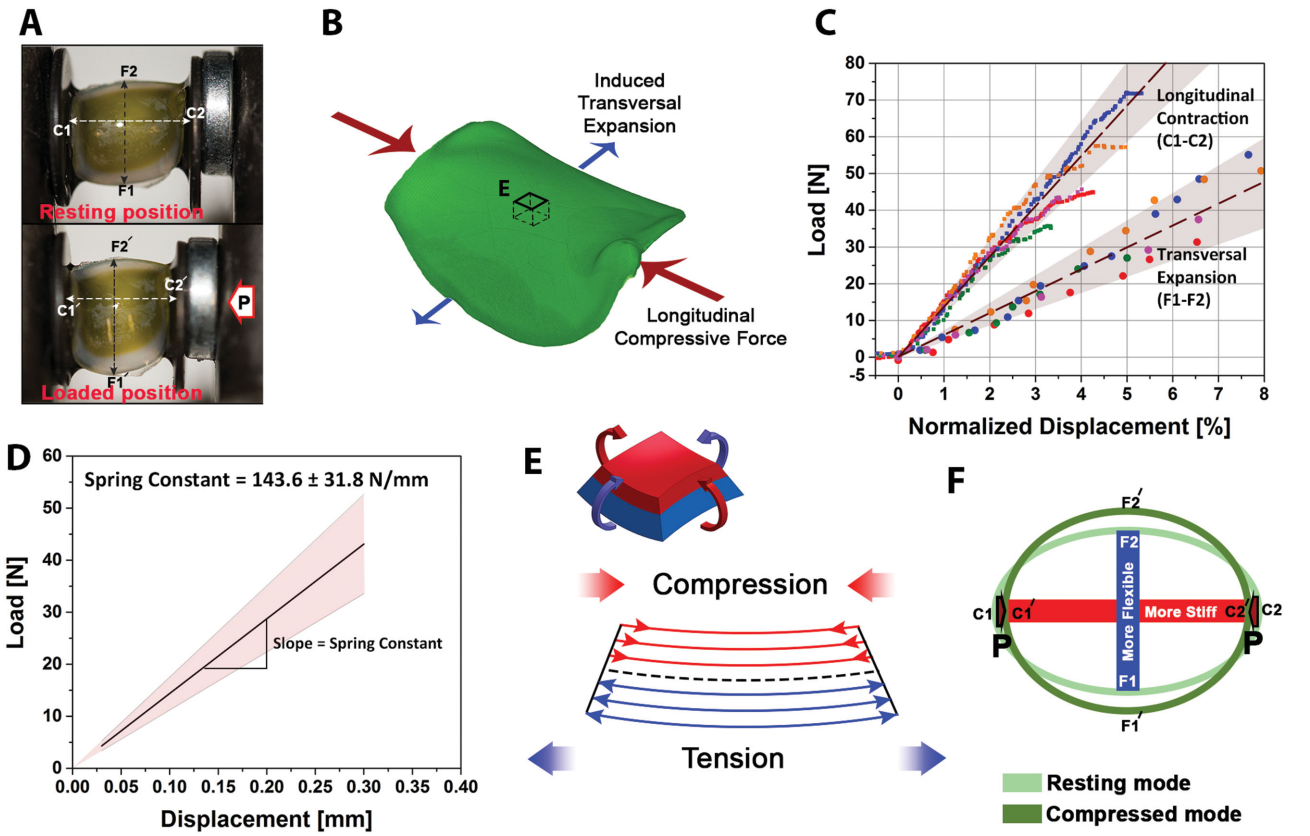

Figure 8. Macroscopic compressive testing of whole saddles. A) Macrophotograph of a saddle in the testing machine in the unloaded (top) and loaded (bottom) states. The load was applied along the longitudinal C1–C2 direction. B) Schematic representation of a saddle during testing. During compression in the longitudinal direction (C1–C2), the saddle expands in the transverse (F1–F2) direction, leading to macroscopic flattening of the structure. C) Compression test results of five saddle samples until failure, associated with deviation from linearity. Lateral expansion during testing is ≈2.5-fold larger (smaller slope) than the longitudinal contraction. D) Average spring constant of saddles, with the shaded area representing the range of values measured for all samples ($n = 25$). E) Volume element from the central region of the saddle, with corresponding stress distribution during saddle bending. Note that this stress distribution will be different near the transverse edges, where expansion will be associated with tensile stresses of the outer surfaces. F) 2D projection (top view) of a saddle showing the contraction/expansion of the main axes during compressive testing. The compressive stiffness in the longitudinal direction is larger than the tensile stiffness in the transverse direction.

organization, relative content of organic/inorganic components, and molecular-scale interfaces precisely tuned to meet their load-bearing functionality.[41] The saddle material is no exception; however its specific biomechanical function cannot be achieved alone with a homogeneous distribution of building blocks, even if these are sophisticated hierarchical composite elements. If the saddle was solely made of the biomineralized composite from the outer layer, it is very likely that the inner layers would prematurely fail due to the relative brittleness of mineralized phases under tensile load regimes. On the other hand, a predominantly organic structure such as that comprising the inner layer would not be able to store a sufficient amount of elastic energy since its elastic modulus is about 6-times lower than the outer mineralized composite.

Therefore, to meet these seemingly exclusive requirements (high stiffness and extensibility with minimization of internal damage), our results show that the spatial distribution of saddle building blocks is precisely tuned. MicroCT scans of the whole saddle combined with FESEM observations and confocal Raman imaging show that the outer layer is more mineralized (84 wt%), with the mineral phases consisting of both fluorinated ACP and Mg-rich ACC (Figure 4), whereas the inner layer is more organic and made of α-chitin and proteins enriched in hydrophobic residues (Figure 6 and Table 1). Micro-mechanical mapping confirms that the outer layer is stiffer than the inner layer, with larger differences in mechanical properties observed under hydrated conditions (Figure 7). This spatial organization has been optimized to take advantage of the intrinsic mechanical characteristics of the structure building blocks. Owing to their much lower susceptibility to microflaws (Griffith fracture) under compressive stresses, minerals are much stronger when subjected to compressive than to tensile loading.[42] Hence depositing a larger mineral content in the outer layers that are under compressive stresses allows stomatopods to maximize the spring stiffness of their saddle, while at the same time minimizing risks of failure. The inner layers, on the other hand, sustain tensile stresses, a loading regime under which biopolymeric materials are more suitable than highly mineralized phases. This requirement is met by the prevalence of an α-chitin/protein complex in this layer. Saddle compression also results in flattening of the structure due to expansion in the lateral direction (Figure 8), leading the

lateral extremities of the saddle to also sustain tensile stresses during bending. Just like along the central cross-sections, the organic/inorganic ratio has been spatially tuned to ensure that the lateral extremities are also predominantly biopolymeric, as observed on both microCT (Figure 2C) and large view FESEM images (Figure 3B). This overall multiscale design allows the saddle to maximize its elastic storage capability, while at the same time minimizing the risks of macroscopic failure.

The identification of the structural proteins involved in the chitin/protein complex will be critical to better understand the mechanisms of tensile elasticity in the inner layers. Although full-length sequences of these proteins remain currently unknown, some clues can be gathered from the global amino acid composition. A high content of Gly is a common hallmark of extracellular elastic proteins such as elastin, abductin, or resilin.[43] Enrichment in both Ala and Gly residues is also a notable feature of load-bearing proteins such as silks[44] or more recently discovered suckerins from the squid sucker ring teeth,[45,46] with Ala-rich domains favoring the formation of stiff β-sheet domains. Resilin is a classical elastic protein that has notably been identified in the hinges of insect wings;[47] however its relatively low Ala and Val content (<7 and <4 mol%, respectively),[48] makes it an unlikely candidate given the higher abundance of these residues in the stomatopod's saddle (Table 1). Likewise abductin that provides the elasticity of bivalve mollusks hinge ligaments contains an unusually high amount of methionine (Met) (≈15 mol%),[49] which is incompatible with the trace amount of Met in the saddle proteins. More recently, it has been established that chitin associates with chitin-binding proteins in softer regions of the robust squid beak[50] to form a relatively hydrophilic biopolymeric complex in these regions, and the sequences of these chitin-binding proteins has been elucidated.[51] We anticipate that a similar complex exists in the saddle inner layers, but this will require further investigations. While such studies have historically proved challenging because of the difficulty in extracting proteins from mineralized structures in high yield and because of the lack of sequenced genomes for most crustaceans,[52] recent advances in combining high-throughput sequencing with proteomics[45] will greatly facilitate such endeavor.

4. Conclusions

The mantis shrimp raptorial appendage has gathered recent interest as a model biological structure in bioinspired materials engineering. This study has focused on the multiscale design of the saddle structure, a main component of the power amplification system allowing the animal to deploy its raptorial appendage at high speed. The saddle functionality requires properties that are apparently mutually exclusive, namely, high stiffness, extensibility, and fatigue resistance. To meet these requirements, the saddle is constructed from building blocks spatially distributed within the structure in a way that exploit their intrinsic mechanical properties. Regions loaded in compression are predominantly made of amorphous mineral phases, whereas regions subjected to tensile loads contain a higher biopolymeric content. The study provides useful lessons for the design of multimaterials bioinspired structures that are both stiff and extensible. Future investigations will aim at establishing structure/property relationships of other elements of the merus structure. Once such precise relationships will have been established, whole simulations of the entire amplification system will be possible by finite element modeling. Another area of interest will be the actual identification and sequencing of elastic proteins located in the inner regions of the saddle and their specific interactions with chitin fibrils, which could shed light on the mechanisms of elastic energy storage at the molecular scale.

5. Experimental Section

Research Specimens (Saddle): Fresh specimens of *Harpiosquilla harpax* (spearer) (Figure 1) and *Odontodactylus scyllarus* (smasher) were obtained from local markets in Singapore and their appendages were immediately dissected and stored at −20 °C. The saddles were dissected with a surgical scalpel and rinsed in deionized water to remove the residual salt and any other organic debris. The samples were embedded in epoxy cold mounting resin (EpoFix Kit, Struers, Denmark), vacuum dried, cut by a linear precision diamond saw IsoMet 4000 (Buehler, USA), grounded on P1200/4000 grade SiC paper, and finally polished with 1 µm and 40 nm diamond paste and colloidal silica suspension, respectively. To remove diamond paste and wash away debris, polished samples were cleaned in ultrasonic bath for 5 min in 5 to 1 volume ratio of water and ethanol between each polishing step.

Microstructural Imaging and Characterization: Field emission scanning electron microscopy (FESEM) was performed using an FESEM 7600F (JEOL, Japan). Both polished and fracture surfaces of the samples were coated with platinum with an approximate thickness of 5 to 10 nm to prevent surface charging. Imaging was done using a lower secondary electron imaging (LEI) detector at an accelerating voltage of 5 KV. Optical microscopy studies were performed with an Axio Scope.A1 (ZEISS, Germany) optical microscope in bright field in the reflective mode. The merus and saddle images were captured using an EOS 700D camera equipped with an EF 100 Macro lens (Canon, Japan). The microCT scans were obtained using an inspeXio SMX-90CT Plus (Shimadzu, Japan), at a 90 kV voltage and 0.012 mm per pix voxel size. The 3D model and the density filtrations were rendered using VGStudio Max software. Energy dispersive spectroscopy (EDS) measurements were conducted on polished and carbon-coated samples with a Bruker X-Flash energy dispersive spectrometer. EDS mapping was performed at an accelerator voltage of 20 keV.

Biochemical Characterization and Gravimetric Assay: In order to calculate the water content of samples, the initial weight of fresh samples was compared with the weight after freeze drying. Subsequently, experimental samples were treated in 0.1 M EDTA for 7 d, weighed once more after freeze-drying to calculate the mineral content. To selectively dissolve the proteins (but not the chitin), two solutions were used. For the first one, demineralized samples were grounded in liquid N_2 and dissolved in an 8 M urea in 5% acetic acid solution within a homogenizer and centrifuged at 14 000 rpm for 5 min to separate the supernatant from the nondissolved solid residues. For the second solution, the demineralized samples were soaked in an alkaline peroxide solution (mixture of H_2O, 30% H_2O_2, and 10N NaOH, with volume percentages of 92.5%, 5%, 2.5%, respectively) in 70 °**C** until the samples were completely depigmented, according to a procedure described by Miserez et al.[33] After each treatment, FTIR spectroscopy and AAA were performed on both the soluble and insoluble fractions. The solid insoluble fraction after the alkaline peroxidation procedure was rinsed several times with DI water and weighted after freeze-drying to quantify the weight percentage of chitin and protein.

The transmission mode of Bruker FTIR Vertex 70 model was used for analysing demineralized samples in the range of 4000 to 800 cm^{-1} with a resolution of 4 cm^{-1}. The spectra were analyzed using the Bruker OPUS 6 software. Prior to AAA, each sample (both the solid residue

and the supernatant) was acid-hydrolysed in 6M HCl with 5% phenol as an anti-oxidant *in vacuo*. The hydrolysates were flash-evaporated using a speed vacuum (Scan Speed, USA), washing them twice with water and methanol. The proteins were then resuspended in 300 µL of Sample Dilution Buffer (SYKAM, Germany). The samples were centrifuged at 14 rpm for 5 min. The hydrolysis was conducted at 110 °C for 24 h. AAA was conducted using a Ninhydrin-based, post-column derivatization Sykam S 433 AAA. The elution time of the peaks was calibrated by standard amino acid solution. For the chitin elution we used glucosamine (the hydrolysis product of chitin and chitosan) as a standard.

Thermogravimetric analysis (TGA) was also carried out on a freshly dissected saddle, from which the outer and inner layers were carefully separated from each other. Measurements were conducted using a TGA Q500 (TA Instrument, USA) with a mass resolution of 0.1 µg. The experiment was performed at linear heating rate of 5.00 °C min^{-1} in an inert atmosphere from ambient temperature to 900 °C.

Raman Spectroscopy and Imaging: Raman spectrometry of embedded and polished cross-sections was acquired with a confocal Raman microscope (alpha300, WITec, Ulm, Germany) equipped with a 532 nm laser source and a 20X Nikon objective lens with 0.4 numeric aperture (NA) and the lateral resolution of ≈0.61 λ/NA. Initial Raman spectroscopy studies were performed along a saddle cross-section in three different points located in the innermost, inner, and outer layer. Each Raman spectrum was acquired for 90 s using 0.5 s integration time. For Raman imaging the data were acquired using 0.3 s integration time and 1 µm spatial resolution. The WITec Project Plus 2.08 was used for filtering, spectrum processing such as average and baseline subtractions, and analysis. The images were generated by plotting the intensity of the Gaussian fit of the signal corresponding to the wavenumber ranges of phosphate (930–990 cm^{-1}), carbonate (1060–1100 cm^{-1}), and organic matrix (2810–2980 cm^{-1}). All the Raman studies were collected in the range of 400–3500 cm^{-1} to cover the whole range for organic and inorganic components.

Nanoindentation: Indentation studies were conducted on embedded and finely polished samples using a Triboindenter TI-950 Nanomechanical tester (Hysitron, Minneapolis, MN, USA), equipped with a 30 mN standard transducer. A cube corner tip (50–70 nm nominal tip curvature) diamond fluid cell tip was chosen for all experiments. Indentation mapping was done over an area of 80 × 380 µm that included the entire width (380 µm) of the saddle's cross section and the indentation spacing was 8 µm in both dried and hydrated conditions. Indentation experiments were conducted with a maximum force of 1000 and 400 µN for the dry and hydrated conditions, respectively. Loading cycles consisted of a 5 s loading time, 2 s holding at peak force, and 5 s unloading time, with loading rates of 200 and 80 µN s^{-1} for the dried and hydrated conditions, respectively. A 1 µN set point force was used to accurately detect the samples' surfaces.

Compression Studies: To measure the stiffness of whole saddle samples, a custom-made micro uniaxial testing machine was used (Supporting Information, Figure S7). The machine was designed to apply tension/compression loads up to 450 N and the micro-testing machine was designed to conduct experiments in both dry and hydrated conditions The load and displacement were monitored using a LSB200 load cell (FUTEK, USA) and a linear variable displacement transducer (LVDT) (S series, Solartron, UK) with 0.1 N force and 1 µm displacement resolution, respectively. The working distance of the machine was 30 mm. SENSIT test and measurement software (Futek, USA) were used to record the load-displacement data. The load cell and LVDT were calibrated by their respective manufacturers. Fresh samples were longitudinally fixed between the grips with super glue and were left in a water container for 30 min before experiments. The load was increased gradually at a rate of 2 N s^{-1} and the immersed samples were loaded until failure. The linear part of the load-displacement curves were used to calculate the spring constant of the saddle samples. Transversal expansion measurements were obtained using a 1 µm resolution digital micrometer (series 293–230 Mitutoyo, Japan), with the data recorded on the computer using a USB-ITN cable (Mitutoyo, Japan).

Data Analysis and Plotting: Statistical analysis and data plotting were done using the Statplus and OriginPro 9.1 software. A total number of 48 saddle samples were tested in the entire study. All samples were collected from fresh mantis shrimp with fully formed inner layers.

Supporting Information

Supporting Information is available from the Wiley Online Library or from the author.

Acknowledgements

This research was funded by the Singapore National Research Foundation (NRF) through a NRF Fellowship awarded to A.M. M.T. and S.A. were supported by a Singapore International Graduate Award (SINGA fellowship). Ad.M. is grateful for the financial support by the German Research Foundation (DFG) within the priority program 1420. The authors thank Mr. Assaf Cohen for providing access to the microCT equipment.

Received: July 19, 2015
Revised: August 29, 2015
Published online: September 24, 2015

[1] F. R. Schram, *J. Paleontol.* **2007**, *81*, 895.
[2] S. Amini, A. Masic, L. Bertinetti, J. S. Teguh, J. S. Herrin, X. Zhu, H. Su, A. Miserez, *Nat. Commun.* **2014**, *5*, 3187.
[3] J. C. Weaver, G. W. Milliron, A. Miserez, K. Evans-Lutterodt, S. Herrera, I. Gallana, W. J. Mershon, B. Swanson, P. Zavattieri, E. DiMasi, D. Kisailus, *Science* **2012**, *336*, 1275.
[4] S. Amini, M. Tadayon, S. Idapalapati, A. Miserez, *Nat. Mater.* **2015**, *14*, 943.
[5] S. N. Patek, W. L. Korff, R. L. Caldwell, *Nature* **2004**, *428*, 819.
[6] M. deVries, E. Murphy, S. Patek, *J. Exp. Biol.* **2012**, *215*, 4374.
[7] M. Burrows, *Z. Vgl. Physiol.* **1969**, *62*, 361.
[8] S. Patek, R. Caldwell, *J. Exp. Biol.* **2005**, *208*, 3655.
[9] J. Taylor, S. Patek, *J. Exp. Biol.* **2010**, *213*, 3496.
[10] S. Patek, D. Dudek, M. Rosario, *J. Exp. Biol.* **2011**, *214*, 1973.
[11] T. Claverie, E. Chan, S. N. Patek, *Evolution* **2011**, *65*, 443.
[12] S. Patek, M. Rosario, J. Taylor, *J. Exp. Biol.* **2013**, *216*, 1317.
[13] S. N. Patek, B. N. Nowroozi, J. E. Baio, R. L. Caldwell, A. P. Summers, *J. Exp. Biol.* **2007**, *210*, 3677.
[14] T. Zack, T. Claverie, S. Patek, *J. Exp. Biol.* **2009**, *212*, 4002.
[15] J. W. C. Dunlop, R. Weinkamer, P. Fratzl, *Mater. Today* **2011**, *14*, 70.
[16] H. Lichtenegger, A. Reiterer, S. E. Stanzl-Tschegg, P. Fratzl, *J. Struct. Biol.* **1999**, *128*, 257.
[17] A. Reiterer, H. Lichtenegger, S. Tschegg, P. Fratzl, *Philos. Mag. A* **1999**, *79*, 2173.
[18] M. A. Meyers, P.-Y. Chen, *Biological Materials Science*, Cambridge University Press, Cambridge, UK, **2014**.
[19] P. Y. Chen, A. Y. Lin, J. McKittrick, M. A. Meyers, *Acta Biomater.* **2008**, *4*, 587.
[20] P. Romano, H. Fabritius, D. Raabe, *Acta Biomater.* **2007**, *3*, 301.
[21] A. Al-Sawalmih, C. H. Li, S. Siegel, H. Fabritius, S. B. Yi, D. Raabe, P. Fratzl, O. Paris, *Adv. Funct. Mater.* **2008**, *18*, 3307.
[22] H.-O. Fabritius, C. Sachs, P. R. Triguero, D. Raabe, *Adv. Mater.* **2009**, *21*, 391.
[23] Z. Movasaghi, S. Rehman, I. U. Rehman, *Appl. Spectrosc. Rev.* **2007**, *42*, 493541.
[24] H. Tsuda, J. Arends, *J. Dental Res.* **1994**, *73*, 1703.
[25] D. Wang, L. M. Hamm, R. J. Bodnar, P. M. Dove, *J. Raman Spectrosc.* **2012**, *43*, 543.

[26] A. Masic, J. C. Weaver, *J. Struct. Biol.* **2015**, *189*, 269.
[27] S. Schrof, P. Varga, L. Galvis, K. Raum, A. Masic, *J. Struct. Biol.* **2014**, *187*, 266.
[28] Niranjan D. T. Parab, V. Tomar, *J. Nanomed. Nanotechnol.* **2012**, *3*, 1.
[29] Y. Politi, D. R. Batchelor, P. Zaslansky, B. F. Chmelka, J. C. Weaver, I. Sagi, S. Weiner, L. Addadi, *Chem. Mater.* **2010**, *22*, 161.
[30] E. Loste, R. M. Wilson, R. Seshadri, F. C. Meldrum, *J. Cryst. Growth* **2003**, *254*, 206.
[31] F. Macchi, F. Shen, R. Keck, R. Harris, in *Amino Acid Analysis Protocols*, Vol. 159 (Eds: C. Cooper, N. Packer, K. Williams), Humana Press, Totwa, NJ, USA **2000**, pp. 9–30.
[32] M. Rinaudo, *Prog. Polym. Sci.* **2006**, *31*, 603.
[33] A. Miserez, T. Schneberk, C. Sun, F. W. Zok, J. H. Waite, *Science* **2008**, *319*, 1816.
[34] G. Falini, S. Albeck, S. Weiner, L. Addadi, *Science* **1996**, *271*, 67.
[35] A. M. Belcher, X. H. Wu, R. J. Christensen, P. K. Hansma, D. E. Morse, *Nature* **1996**, *281*, 56.
[36] A. George, A. Veis, *Chem. Rev.* **2008**, *108*, 4670.
[37] M. Suzuki, K. Saruwatari, T. Kogure, Y. Yamamoto, T. Nishimura, T. Kato, H. Nagasawa, *Science* **2009**, *325*, 1388.
[38] S. Amini, A. Miserez, *Acta Biomater.* **2013**, *9*, 7895.
[39] S. Ruangchai, C. Reisecker, S. Hild, A. Ziegler, *J. Struct. Biol.* **2013**, *182*, 22.
[40] J. W. C. Dunlop, P. Fratzl, *Annu. Rev. Mater. Res.* **2010**, *40*, 1.
[41] P. Laaksonen, G. R. Szilvay, M. B. Linder, *Trends Biotechnol.* **2012**, *30*, 191.
[42] P.-Y. Chen, J. McKittrick, M. A. Meyers, *Prog. Mater. Sci.* **2012**, *57*, 1492.
[43] A. S. Tatham, P. R. Shewry, *Philos. Trans. R. Soc., B* **2002**, *357*, 229.
[44] J. M. Gosline, P. A. Guerette, C. S. Ortlepp, K. N. Savage, *J. Exp. Biol.* **1999**, *202*, 3295.
[45] P. A. Guerette, S. Hoon, Y. Seow, M. Raida, A. Masic, F. T. Wong, V. H. Ho, K. W. Kong, M. C. Demirel, A. Pena-Francesch, S. Amini, G. Z. Tay, D. Ding, A. Miserez, *Nat. Biotechnol.* **2013**, *31*, 908.
[46] P. A. Guerette, S. Hoon, D. Ding, S. Amini, A. Masic, V. Ravi, B. Venkatesh, J. C. Weaver, A. Miserez, *ACS Nano* **2014**, *8*, 7170.
[47] T. Weis-Fogh, *J. Exp. Biol.* **1960**, *37*, 889.
[48] D. H. Ardell, S. O. Andersen, *Insect Biochem. Mol. Biol.* **2001**, *31*, 965.
[49] Q. Cao, Y. Wang, H. Beyley, *Curr. Biol.* **1997**, *7*, R677.
[50] D. Rubin, A. Miserez, J. H. Waite, in *Advances in Insect Physiology*, Vol. 38 (Eds: J. Casas and S. Simpson), Elsevier Science, **2010**, pp. 75–133, Oxford, U.K.
[51] Y. Tan, S. Hoon, P. A. Guerette, W. Wei, A. Ghadban, C. Hao, A. Miserez, J. H. Waite, *Nat. Chem. Biol.* **2015**, *11*, 488.
[52] J. Trapp, C. Almunia, J. C. Gaillard, O. Pible, A. Chaumot, *J. Proteomics* **2015**.